Real-space imaging of the atomic-scale magnetic structure of $Fe_{1+y}Te$

Mostafa Enayat,[1]* Zhixiang Sun,[1]* Udai Raj Singh,[1] Ramakrishna Aluru,[1] Stefan Schmaus,[1] Alexander Yaresko,[1] Yong Liu,[1]† Chengtian Lin,[1] Vladimir Tsurkan,[2,3] Alois Loidl,[2] Joachim Deisenhofer,[2] Peter Wahl[1,4]‡

Spin-polarized scanning tunneling microscopy (SP-STM) has been used extensively to study magnetic properties of nanostructures. Using SP-STM to visualize magnetic order in strongly correlated materials on an atomic scale is highly desirable, but challenging. We achieved this goal in iron tellurium ($Fe_{1+y}Te$), the nonsuperconducting parent compound of the iron chalcogenides, by using a STM tip with a magnetic cluster at its apex. Our images of the magnetic structure reveal that the magnetic order in the monoclinic phase is a unidirectional stripe order; in the orthorhombic phase at higher excess iron concentration ($y > 0.12$), a transition to a phase with coexisting magnetic orders in both directions is observed. It may be possible to generalize the technique to other high-temperature superconductor families, such as the cuprates.

In many strongly correlated high-temperature superconductors (HTSCs), the nonsuperconducting parent compound is in an antiferromagnetically ordered state, which becomes superconducting upon chemical doping. This is true for most of the iron-based HTSCs (*1*–*3*) and for copper oxide–based materials (*4*). Establishing the relation between magnetic order and superconductivity is thought to be key to understanding the physics of these materials. Magnetic order in strongly correlated electron materials is usually observed by means of neutron scattering. Real-space imaging of magnetic order is possible in principle with spin-polarized scanning tunneling microscopy (SP-STM), which has been used extensively to study magnetic properties of thin films, nanostructures, and magnetic clusters (*5*–*7*). Yet, application to strongly correlated electron systems has remained scarce (*7*). The experimental challenge lies in identifying a suitable procedure for preparing a STM tip that yields magnetic contrast.

Iron tellurium ($Fe_{1+y}Te$) is the nonsuperconducting parent compound of the iron chalcogenide superconductors, in which superconductivity is induced by the substitution of Te with Se (*8*). The parent compound exhibits a bicollinear stripe magnetic order with a wave vector (1/2, 0, 1/2) [defined in the two iron unit cell (Fig. 1A)] (*9*–*11*). The magnetic order sets in at a temperature of ~60 to 70 K, accompanied by a structural phase transition, with the structure changing from tetragonal to monoclinic. With increasing concentration y of excess iron, the transition temperature is reduced, and the magnetic and structural transitions are separated (*12*, *13*). At excess iron concentrations of $y > 0.12$, the crystal structure becomes orthorhombic (*13*), and the magnetic order becomes incommensurate with the lattice (*11*). The magnetic structure is distinct from the one found in the parent compounds of the iron-pnictide superconductors. The absence of nesting at the wave vector of the magnetic order suggests that local moments and their interactions are important. Density functional theory (DFT) calculations reproduce the magnetic structure at $y = 0$ (*14*, *15*). Several microscopic Heisenberg models have been proposed to describe the magnetic order in the FeTe plane and the spin excitations (*15*–*19*), but mapping onto a Heisenberg model remains controversial (*20*).

Because of their layered structure, electronic properties and magnetism in iron-pnictides and -chalcogenides are quasi–two-dimensional (*3*), making them ideally suited for a study by means of SP-STM. The magnetic interactions in $Fe_{1+y}Te$ are predominantly two-dimensional within the FeTe-plane; hence, we consider in the following only the in-plane component of the magnetic order.

Here, we report an investigation by means of SP-STM of the real-space magnetic structure at the atomic scale of $Fe_{1+y}Te$. Our STM data were obtained with a tip that has a magnetic cluster at its apex (Fig. 1B) [(*21*), section S1B]. In a topographic image of the sample surface obtained with a tip that does not yield magnetic contrast (Fig. 1C), the square lattice can be identified from its lattice constant as the top-layer tellurium atoms. Excess iron atoms at the surface show up as bright protrusions (*22*–*24*). The Fourier transform of the topography clearly shows the peaks associated with the tellurium lattice at the surface. The two nonequivalent spots at $\mathbf{q}^{a}_{\mathrm{Te}} = (\pm 1, 0)$ and $\mathbf{q}^{b}_{\mathrm{Te}} = (0, \pm 1)$ have noticeably different intensities. A topographic image obtained with a tip that yields magnetic contrast for the same area as in Fig. 1C is shown in Fig. 1D. It shows clear stripe-like patterns superimposed to the atomic lattice. The stripes result from spin-polarized tunneling into regions with a spin-polarization parallel or antiparallel to that of the tip, imaged higher or lower, respectively. The unidirectional modulation has two major components in the Fourier transform: The first is a pair of distinct peaks at wave vectors $\mathbf{q}_{\mathrm{AFM}} = (\pm 1/2, 0)$; the second, which is also seen with a nonmagnetic tip, at $\mathbf{q}_{\mathrm{CDW}} = (\pm 1, 0)$ coincides with the atomic peak of the tellurium lattice. Antiferromagnetic or spin density wave (SDW) order is expected to be accompanied by a charge density wave (CDW) (*25*, *26*) with twice the wave vector of the magnetic order ($\mathbf{q}_{\mathrm{CDW}} = 2\mathbf{q}_{\mathrm{AFM}}$), which is consistent with our data. A superposition of a sketch of the magnetic structure with a topographic image is shown in Fig. 1E.

[1]Max-Planck-Institut für Festkörperforschung, Heisenbergstrasse 1, D-70569 Stuttgart, Germany. [2]Center for Electronic Correlations and Magnetism, Experimental Physics V, University of Augsburg, D-86159 Augsburg, Germany. [3]Institute of Applied Physics, Academy of Sciences of Moldova, MD 2028, Chisinau, Republica Moldova. [4]Scottish Universities Physics Alliance, School of Physics and Astronomy, University of St. Andrews, North Haugh, St. Andrews, Fife KY16 9SS, UK.
*These authors contributed equally to this work. †Present address: Division of Materials Sciences and Engineering, Ames Laboratory, U.S. Department of Energy, Ames, IA 50011, USA. ‡**Corresponding author. E-mail: gpw2@st-andrews.ac.uk**

The modulation caused by the antiferromagnetic order was observed consistently over large surface areas and was never found to switch direction within a domain of the monoclinic distortion in samples with low excess iron concentration ($y < 0.12$); only at domain boundaries do the stripes switch direction (Fig. 1F).

Calculations (fig. S1) [(*21*), section S1C] show that in addition to the Fe atoms, the electronic states at the Te sites are also strongly spin-polarized in the vicinity of the Fermi level, with the direction of the induced magnetization of the Te atoms being in plane and in opposite direction to the spin of the three equal-spin iron neighbors. According to the topographic contrast (up to ~20 pm between equivalent sites), the spin-polarization of the tunneling current is up to 20%. This would be consistent with the calculated spin-polarization on either the iron or tellurium atoms when the polarization of the tip is assumed to be similar to that of an iron-coated tip (*27*). The magnetic peaks we observe at $\mathbf{q}_{AFM}$ likely contain contributions from both.

To verify that the stripe modulation originates from spin-polarized tunneling, we performed measurements in magnetic field. Even in the presence of the field applied almost perpendicular to the sample surface, the magnetization of the tip is not perfectly perpendicular to the sample surface, enabling us to probe its in-plane magnetic texture [(*21*), section 1D]. Topographic images taken at the same location on the surface in magnetic fields of $B = +5$T and -5T are shown in Fig. 2, A and B, respectively. The stripes shift by half the wavelength of the antiferromagnetic order upon reversing the direction of the magnetic field. This can be clearly seen in the line profiles along the a direction (Fig. 2C, top), which were obtained from Fig. 2, A and B, by averaging along the stripes of the modulation (parallel to the b direction). The magnetic field dependence of the imaging contrast demonstrates that the stripe modulation is due to spin-polarized tunneling. The antiferromagnetic coupling between the spins on the iron atoms and an appreciable magneto-crystalline anisotropy of ~0.5 meV/Fe (estimated from DFT calculations) prevent the spins in the sample from aligning with the external magnetic field; the field switches the magnetization of the apex of the tip only. The atomic registry of the topographies in Fig. 2, A and B, allows us to separate magnetic from topographic information and extract the spin polarization of the tunneling current [(*21*), section S2]. The average of the two images yields a spatial map of the nonmagnetic contrast (Fig. 2C, bottom, black line; and 2D), whereas the difference yields the magnetic contrast only (Fig. 2C, bottom, red line; and 2E). The line profiles in Fig. 2C reveal that the strongest spin polarization is observed in between the tellurium atoms, indicating that the dominant contribution to the magnetic contrast comes from direct tunneling to the iron d-states. The appearance of excess iron atoms shows a strong dependence on the spin-polarization of the tip (Fig. 2, A, B, and F). The topographic height of the excess iron atoms is directly correlated with the apparent height of the trough between two rows of tellurium atoms, both switching their apparent height with field. Line cuts through two defects with opposite spin polarization are plotted in Fig. 2F, top, one imaged high and the other low at 5T and vice versa at -5T. Assuming that for both, tunneling occurs predominantly into a minority state, the spin of the excess iron atoms is parallel to the one of its three equal-spin neighbors (Fig. 2G). This is confirmed with DFT calculations, which show that this configuration is the energetically favorable one and the states at the Fermi energy are predominantly of minority character (fig. S2) [(*21*), section S1C]. A plot of the spin

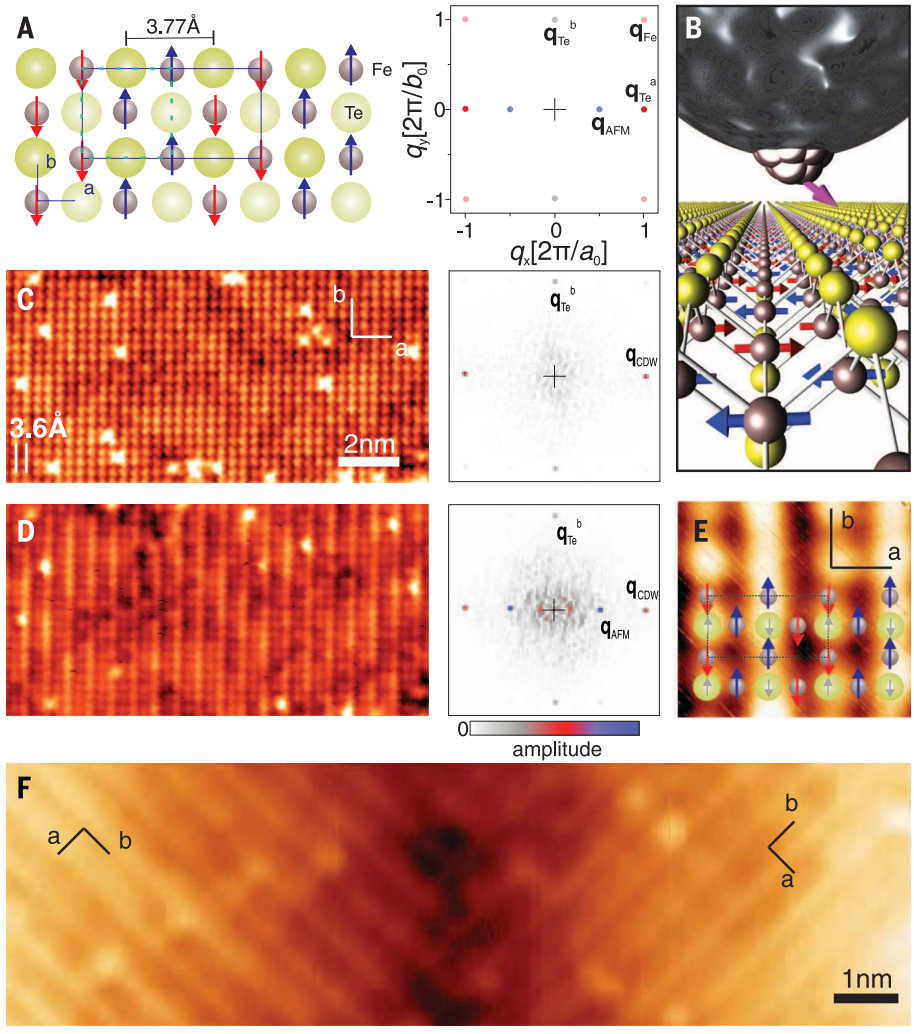

Fig. 1. Magnetic order in FeTe and its detection in STM. (**A**) Schematic of the nonmagnetic (dashed lines) and magnetic unit cell (solid lines) of FeTe. (Right) The expected pattern in a Fourier transformed topographic image owing to the top-layer Te atoms, the Fe square lattice, and the magnetic order. (**B**) Schematic of spin-polarized STM measurement on FeTe, with a nonmagnetic tip that has a small magnetic iron or $Fe_{1+y}Te$ cluster at its apex. (**C**) Topography $z(\mathbf{x})$ of a $Fe_{1+y}Te$ sample with $y = 0.08$ acquired with a tip that shows no magnetic contrast. Excess iron atoms show up as protrusions ($V_b = 60$ mV, $I_t = 200$ pA, $T = 3.8$ K). The Fourier transform of the topography (right) $\tilde{z}(\mathbf{q})$ shows the peaks associated with the Te lattice at $\mathbf{q}_{Te}^{a} = (\pm 1, 0)$ and $\mathbf{q}_{Te}^{b} = (0, \pm 1)$. One pair of peaks at $\mathbf{q}_{CDW} (= \mathbf{q}_{Te}^{a})$ shows up with stronger intensity than the other. (**D**) Topography acquired in the same area as (C) with a tip that shows magnetic contrast ($V_b = 60$ mV, $I_t = 200$ pA, $T = 3.8$ K). The Fourier transform (right) shows additional peaks associated with magnetic order at $\mathbf{q}_{AFM} = (\pm 1/2, 0)$. (**E**) Ball model of the top-most tellurium and iron atoms overlayed on a topographic image. Arrows on Te atoms indicate calculated spin polarization; arrows on iron atoms indicate the local magnetic moment obtained from neutron scattering (*11*). Because the direction of the magnetization of the tip is unknown, a magnetic structure with all spins reversed can yield the same contrast ($V_b = 50$ mV, $I_t = 500$ pA, $T = 30$ mK). (**F**) Topographic image of a twin boundary. The stripes in the two domains are perpendicular to each other ($V_b = 150$ mV, $I_t = 30$ pA, $T = 30$ mK).

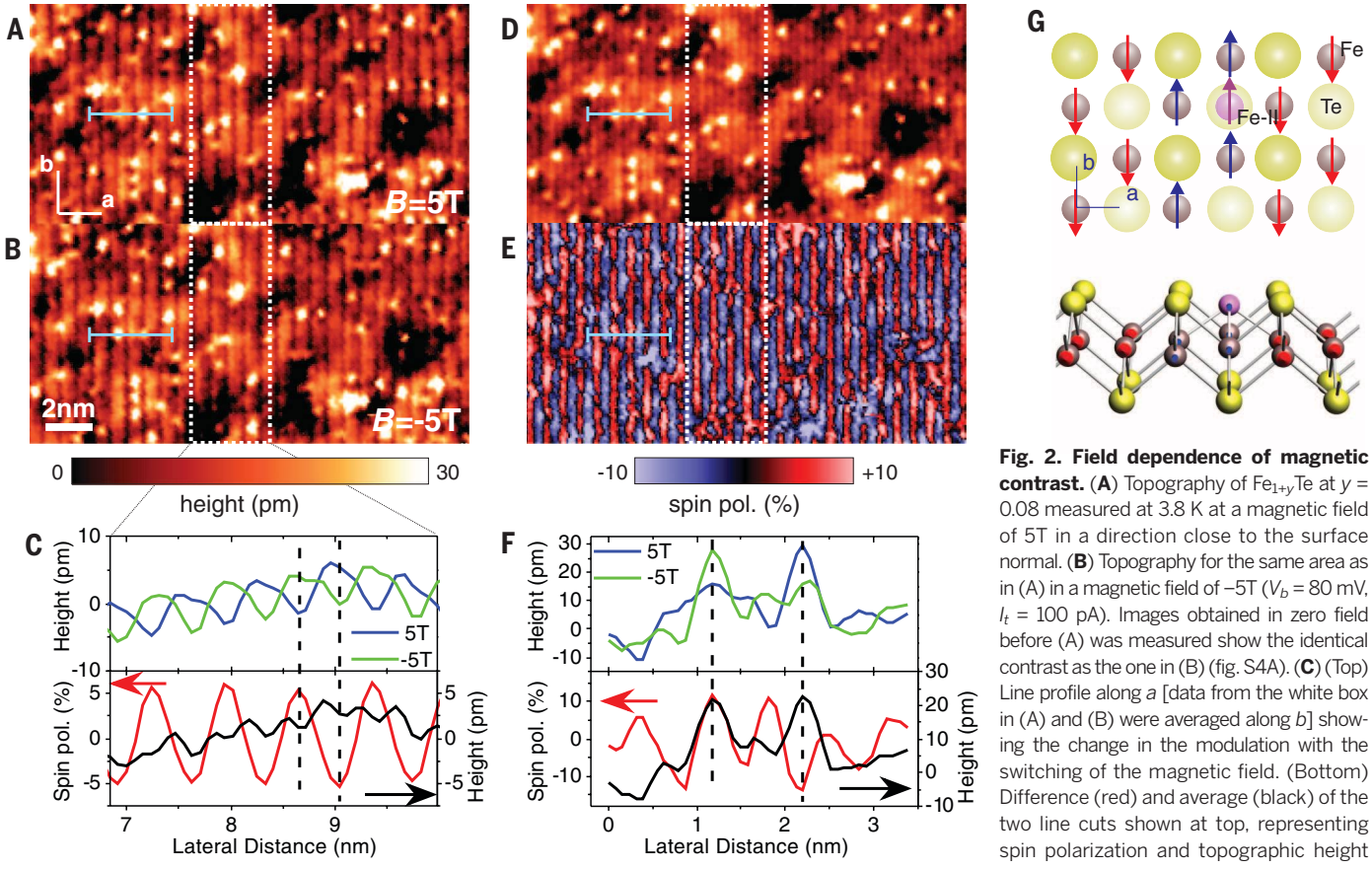

Fig. 2. Field dependence of magnetic contrast. (**A**) Topography of $Fe_{1+y}Te$ at y = 0.08 measured at 3.8 K at a magnetic field of 5T in a direction close to the surface normal. (**B**) Topography for the same area as in (A) in a magnetic field of –5T (V_b = 80 mV, I_t = 100 pA). Images obtained in zero field before (A) was measured show the identical contrast as the one in (B) (fig. S4A). (**C**) (Top) Line profile along *a* [data from the white box in (A) and (B) were averaged along *b*] showing the change in the modulation with the switching of the magnetic field. (Bottom) Difference (red) and average (black) of the two line cuts shown at top, representing spin polarization and topographic height along the profile, respectively. The spin polarization is obtained as described in (*21*), section S2. Vertical dashed lines mark positions of largest positive and negative spin polarization. (**D**) Average of the images in (A) and (B) showing the topography as it would be obtained with a nonmagnetic tip. (**E**) Map of spin polarization obtained from the difference of the images in (A) and (B). (**F**) (Top) Line cut through a pair of excess iron defects that have different spin-polarization [taken at light-blue solid line in (A) and (B)]. (Bottom) Profile of spin polarization (red) and topography (black) along the line cut [light blue solid line in (D) and (E)]. Vertical dashed lines mark positions of the two excess iron atoms. (**G**) Model of an excess Fe atom (pink) on an FeTe layer with the spin-structure deduced from our data. The excess iron atom is marked Fe-II. It resides between four tellurium atoms.

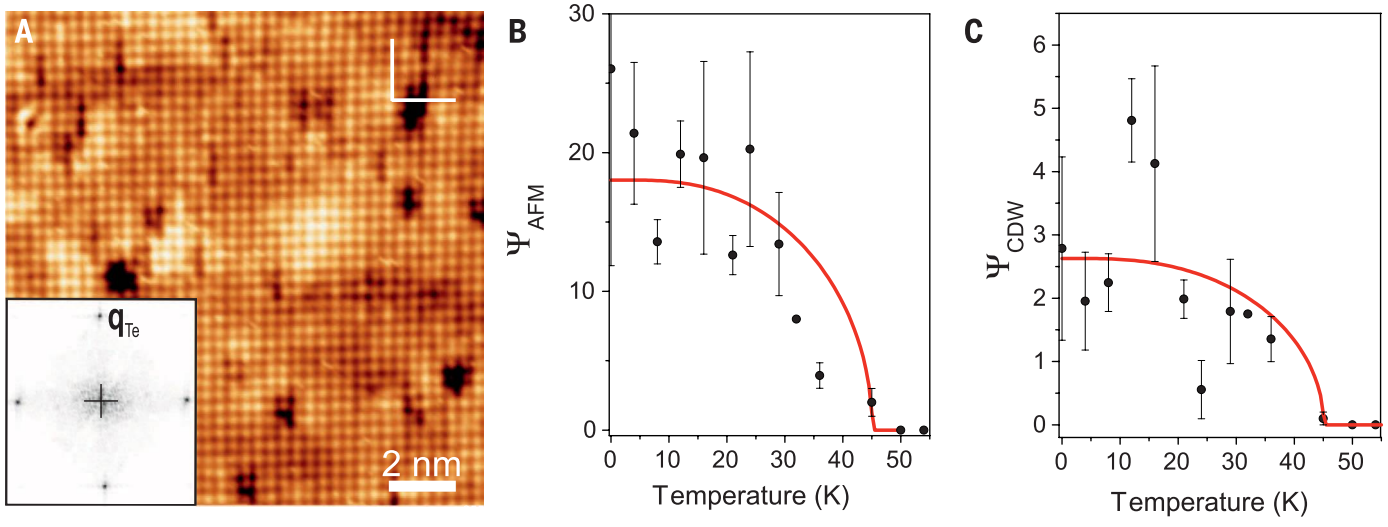

Fig. 3. Temperature dependence of magnetic contrast. (**A**) Topography of $Fe_{1+y}Te$ at y = 0.08 recorded at 54 K. (Inset) The Fourier transform of the topography. The unidirectional modulation is not detected at this temperature (V_b = 100 mV, I_t = 800 pA). (**B**) Intensity $\psi_{AFM} = \tilde{z}(\mathbf{q}_{AFM})/\tilde{z}(\mathbf{q}^{b}_{Te})$ at the wave vector of the spin density wave $\mathbf{q}_{AFM}$ as a function of temperature. Error bars are obtained from the SD from the mean. Solid red line is a fit of mean field theory $[\psi(T) = \psi_0 \tanh\left(\frac{\pi}{2}\sqrt{\frac{T_c}{T} - 1}\right)$ (*35*, *36*)]. (**C**) Intensity $\psi_{CDW} = [\tilde{z}(\mathbf{q}_{CDW}) - \tilde{z}(\mathbf{q}^{b}_{Te})]/\tilde{z}(\mathbf{q}^{b}_{Te})$ analyzed from the same data set as (B) at the wave vector of the charge density wave $\mathbf{q}_{CDW}$ as a function of temperature. For the fit in (C), T_c was fixed at the same value as in (B).

polarization across the two excess iron atoms (Fig. 2F, bottom) shows that the magnetic contrast found on and near excess iron atoms is enhanced.

Our data at low temperature show the same periodicity of the magnetic order as found in neutron scattering. In order to establish the relation of the magnetic modulation to the magneto-structural phase transition observed in the bulk, we studied its temperature dependence. Upon increasing the temperature, the stripe modulation disappeared around a temperature T of 45 K and was not observed at $T > 50$ K. The Fourier transform of a topographic image taken at $T = 54$ K (Fig. 3A) shows only the peaks associated with the Te lattice. To quantify the intensity of the modulation, we used the ratio $\psi_{AFM} = \tilde{z}(\mathbf{q}_{AFM})/\tilde{z}(\mathbf{q}^b_{Te})$, whose temperature dependence shows a trend consistent with a mean-field behavior with a critical temperature $T_c = 45$ K (Fig. 3B). A priori, it is not clear whether the disappearance of the magnetic contrast is related to the transition to the paramagnetic phase of the sample or to a loss of spin-polarization of the tip. This can be clarified by analyzing the CDW modulation, which accompanies the antiferromagnetic order and can be detected with both magnetic and nonmagnetic tips. In Fig. 3C, we plot $\psi_{CDW} = [\tilde{z}(\mathbf{q}_{CDW}) - \tilde{z}(\mathbf{q}^b_{Te})]/\tilde{z}(\mathbf{q}^b_{Te})$ for the same data as in Fig. 3B as a function of temperature. It shows a similar temperature dependence as that of ψ_{AFM}; therefore, the magnetic order at the sample surface sets in at a lower temperature than in the bulk, where the transition temperature is 60 to 70 K. A possible explanation is that the surface $Fe_{1+y}Te$ layer has only one neighboring layer, as opposed to two in the bulk.

The magnetic order in $Fe_{1+y}Te$ becomes more complex with increased excess iron content y (*11*, *28*). A topographic image obtained on a sample with $y = 0.15$ (Fig. 4) reveals stripelike patterns in both directions, at (±1/2, 0) and (0, ±1/2) in Fourier space (Fig. 4A, inset), coexisting in the same domain of the orthorhombic distortion. The image reveals nanoscale domains of predominantly unidirectional stripes coexisting with regions of bidirectional patterns. These two-dimensional patterns could be caused by a superposition between the two unidirectional modulations or by a transition toward a plaquette order, which has been theoretically predicted to become more important as the sample becomes orthorhombic (*19*). The magnetic structure appears still locally commensurate with the lattice, but there are phase slips between different nanoscale domains. This can be more clearly seen from a Fourier-filtered image in which only the Fourier components associated with the magnetic contrast are shown (Fig. 4B).

Our observation of a unidirectional stripelike magnetic order in the monoclinic phase indicates that the monoclinic distortion suppresses bidirectional or plaquette magnetic order at low excess iron concentrations, strongly favoring unidirectional stripe order. As the lattice constants in the *a*- and *b*-direction approach each other with increasing excess Fe concentration (*11*, *29*), we observe both directions of the magnetic order near (±1/2, 0) and (0,±1/2) coexisting in the same domain of the sample, with patches reminiscent of plaquette order. Further, the magnetic order becomes incommensurate. Noncommensurate magnetic order has also been detected in neutron scattering at high excess iron concentrations, showing a shortening of the wave vector associated with the magnetic order (*11*, *28*). In our case, the peak associated with the magnetic order spreads away from the high-symmetry direction. Because the material still has an orthorhombic distortion, the two directions will not have the same energetics, which raises interesting questions as to how the magnetic order sets in as a function of temperature. For high excess iron concentrations $y \gtrsim 0.12$, evidence for an additional magnetically ordered phase has been reported (*13*, *28*, *29*).

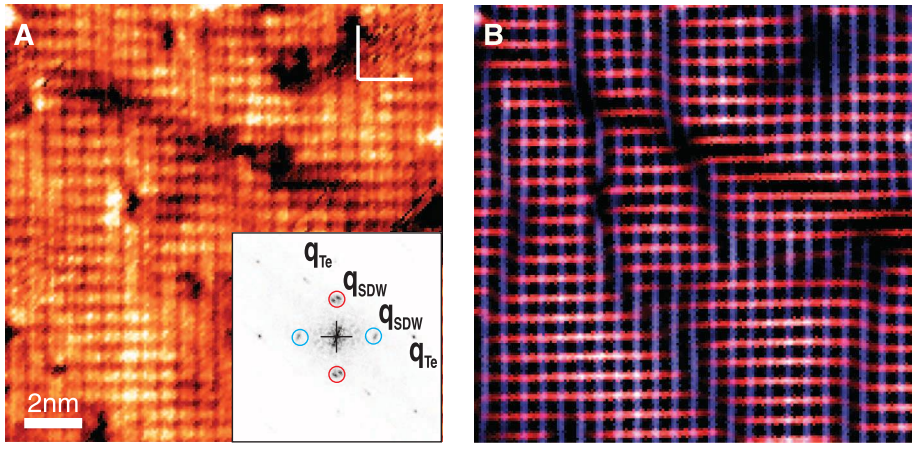

Fig. 4. Magnetic structure at higher excess iron concentration ($y > 0.12$). (**A**) Topography obtained from a sample with high excess iron concentration ($y = 0.15$), showing stripe modulation in two directions superimposed ($V_b = 100$ mV, $I_t = 100$ pA, $T = 1.8$ K). A large part of excess iron has been picked up by the tip, leaving an almost clean Te-terminated surface. (Inset) Fourier transform of the topography showing peaks associated with magnetic contrast around (±1/2, 0) and (0, ±1/2). (**B**) Filtered image showing the components associated with magnetic contrast in different colors in order to visualize the bidirectional stripe order.

Our work brings into reach the possibility to obtain real-space images of stripe order in cuprates (*30*–*32*) and search for magnetic order accompanying the spatially modulated electronic states found in the pseudogap phase (*33*, *34*).

REFERENCES AND NOTES

1. K. Ishida, Y. Nakai, H. Hosono, *J. Phys. Soc. Jpn.* **78**, 062001 (2009).
2. J. Paglione, R. Greene, *Nat. Phys.* **6**, 645–658 (2010).
3. M. D. Lumsden, A. D. Christianson, *J. Phys. Condens. Matter* **22**, 203203 (2010).
4. E. Dagotto, *Science* **309**, 257–262 (2005).
5. R. Wiesendanger, H. Güntherodt, G. Güntherodt, R. J. Gambino, R. Ruf, *Phys. Rev. Lett.* **65**, 247–250 (1990).
6. A. Smith, *J. Scan. Probe Micro.* **1**, 3–20 (2006).
7. R. Wiesendanger, *Rev. Mod. Phys.* **81**, 1495–1550 (2009).
8. Y. Mizuguchi, Y. Takano, *J. Phys. Soc. Jpn.* **79**, 102001 (2010).
9. D. Fruchart *et al.*, *Mater. Res. Bull.* **10**, 169–174 (1975).
10. S. Li *et al.*, *Phys. Rev. B* **79**, 054503 (2009).
11. W. Bao *et al.*, *Phys. Rev. Lett.* **102**, 247001 (2009).
12. A. Martinelli *et al.*, *Phys. Rev. B* **81**, 094115 (2010).
13. S. Rößler *et al.*, *Phys. Rev. B* **84**, 174506 (2011).
14. M. Johannes, I. Mazin, *Phys. Rev. B* **79**, 220510 (2009).
15. F. Ma, W. Ji, J. Hu, Z. Y. Lu, T. Xiang, *Phys. Rev. Lett.* **102**, 177003 (2009).
16. C. Fang, B. Bernevig, J. Hu, *Europhys. Lett.* **86**, 67005 (2009).
17. A. Turner, F. Wang, A. Vishwanath, *Phys. Rev. B* **80**, 224504 (2009).
18. I. A. Zaliznyak *et al.*, *Phys. Rev. Lett.* **107**, 216403 (2011).
19. S. Ducatman, N. B. Perkins, A. Chubukov, *Phys. Rev. Lett.* **109**, 157206 (2012).
20. J. Glasbrenner, J. Velev, I. Mazin, *Phys. Rev. B* **89**, 064509 (2014).
21. Materials and methods are available as supplementary materials on *Science* Online.
22. X. He *et al.*, *Phys. Rev. B* **83**, 220502 (2011).
23. T. Machida *et al.*, *J. Phys. Soc. Jpn.* **81**, 074714 (2012).
24. T. Machida *et al.*, *Phys. Rev. B* **87**, 214508 (2013).
25. O. Zachar, S. Kivelson, V. Emery, *Phys. Rev. B* **57**, 1422–1426 (1998).
26. A. Balatsky, D. Basov, J. Zhu, *Phys. Rev. B* **82**, 144522 (2010).
27. M. Bode, M. Getzlaff, R. Wiesendanger, *Phys. Rev. Lett.* **81**, 4256–4259 (1998).
28. E. Rodriguez *et al.*, *Phys. Rev. B* **84**, 064403 (2011).
29. C. Koz, S. Rößler, A. Tsirlin, S. Wirth, U. Schwarz, *Phys. Rev. B* **88**, 094509 (2013).
30. J. Zaanen, O. Gunnarsson, *Phys. Rev. B* **40**, 7391–7394 (1989).
31. J. Tranquada, B. Sternlieb, J. Axe, Y. Nakamura, S. Uchida, *Nature* **375**, 561–563 (1995).
32. S. Kivelson, E. Fradkin, V. Emery, *Nature* **393**, 550–553 (1998).
33. M. Vershinin *et al.*, *Science* **303**, 1995–1998 (2004).
34. Y. Kohsaka *et al.*, *Science* **315**, 1380–1385 (2007).
35. F. Gross *et al.*, *Z. Phys. B* **64**, 175–188 (1986).
36. D. S. Inosov *et al.*, *Phys. Rev. Lett.* **104**, 187001 (2010).

ACKNOWLEDGMENTS

We acknowledge discussions with S. Chi, M. Etzkorn, F. Kruger, A.P. Mackenzie, S. Rößler, U. Rößler, and M. Ternes. Z.S. acknowledges financial support from Rubicon grant 680.50.1119 (Nederlandse Organisatie voor Wetenschappelijk Onderzoek). V.T., A.L., and J.D. acknowledge financial support from the Deutsche Forschungsgemeinschaft Transregional Research Center TRR80 (Augsburg, Munich, Stuttgart). P.W. acknowledges funding from the Engineering and Physical Sciences Research Council and Max Planck Society.